Computers in Biology and Medicine 196 (2025) 110841

Contents lists available at ScienceDirect

Computers in Biology and Medicine

journal homepage: www.elsevier.com/locate/compbiomed

A hyperspectral imaging dataset and Grassmann manifold method for intraoperative pixel-wise classification of metastatic colon cancer in the liver

Ivica Kopriva [a,*], Dario Sitnik [b,2], Laura-Isabelle Dion-Bertrand [c,1], Marija Milković Periša [d,e], Arijana Pačić [f], Mirko Hadžija [g], Marijana Popović Hadžija [g]

[a] Division of Computing and Data Sciences, Ruđer Bošković Institute, Bijenička cesta 54, Zagreb, Croatia
[b] School of Computation, Information Technology (CIT), Technical University Munich, Arcisstraße 21, 80333, Munich, Germany
[c] Photon etc., 5795 De Gaspe Avenue, Montreal, QC, H2S 2X3, Canada
[d] Clinical Hospital Center Zagreb, Kišpatićeva 12, 10000, Zagreb, Croatia
[e] Institute of Pathology, School of Medicine, University of Zagreb, 10000, Zagreb, Croatia
[f] Department of Pathology and Cytology, Clinical Hospital Dubrava, Avenija Gojka Šuška 6, 10000, Zagreb, Croatia
[g] Division of Molecular Medicine, Ruđer Bošković Institute, Bijenička cesta 54, 10000, Zagreb, Croatia

ARTICLE INFO

Keywords:
Hyperspectral imaging
Intraoperative analysis
Metastatic colon cancer
Liver
Grassmann manifold learning
Tensor spectrum singularity analysis
Deep learning

ABSTRACT

Hyperspectral imaging (HSI) holds significant potential for transforming the field of computational pathology. However, the number of HSI-based research studies remains limited, and in many cases, the advantages of HSI over traditional RGB imaging have not been conclusively demonstrated, particularly for specimens collected intraoperatively. To address these challenges we present: (*i*) a database consisted of 27 HSIs of hematoxylin-eosin stained frozen sections, collected from 14 patients with colon adenocarcinoma metastasized to the liver. It is aimed to validate pixel-wise classification for intraoperative tumor resection; (*ii*) a novel method which combines Grassmann points with nearest subspace classifier for pixel-wise classification of HSIs. The HSIs were acquired in the spectral range of 450 nm–800 nm, with a resolution of 1 nm, resulting in images of 1384 × 1035 pixels. Pixel-wise annotations were performed by two pathologists and one medical expert. To overcome challenges such as experimental variability and the lack of annotated data, we applied Grassmann manifold (GM) approach in combination with spectral-spatial features extracted by tensor singular spectrum analysis (TSSA) method to non-overlapping patches of 230 × 258 pixels. Using only 1 % of labeled pixels per class, the GM-TSSA method achieved a micro balanced accuracy (BACC) of 0.963 and a micro F_1-score of 0.959 on the HSI dataset. The GM-TSSA approach outperformed six deep learning architectures trained with 63 % of labeled pixels. Data are available at: https://data.fulir.irb.hr/islandora/object/irb:538, and code is available at: https://github.com/ikopriva/ColonCancerHSI.

1. Introduction

Segmentation and classification of medical images are crucial for disease diagnosis, therapy planning, follow-up tracking of therapy efficiency, and intraoperative tumor resection. It is known that life expectancy improves with the extensive resection of both primary tumors and their metastasis, such as colon adenocarcinoma in the liver [1]. This also applies to other tumors, including gliomas [2], and oral squamous cell carcinomas [3]. In particular, the margin of non-tumor tissue surrounding the tumor, known as the resection margin [4], is a powerful predictor of the 5-year survival rate [5–7]. However, achieving total resection is challenging due to tumor infiltration into surrounding tissue, making tumor borders difficult to identify. Surgeons rely on intraoperative information provided by pathologists, who perform

* Corresponding author.
E-mail addresses: ikopriva@irb.hr (I. Kopriva), dario.sitnik@gmail.com (D. Sitnik), laura-isabelle.dion-bertrand@umontreal.ca (L.-I. Dion-Bertrand), mmperisa@gmail.com (M.M. Periša), arijanapacic@yahoo.com (A. Pačić), Hadzija.mirko@gmail.com (M. Hadžija), Marijana.Popovic.Hadzija@irb.hr (M.P. Hadžija).
[1] Present address: Department of Physics, University of Montreal, Montreal, Quebec H2C OB3, Canada.
[2] Present address: Preußenstr. 11B, 80809 Munich, Germany.

https://doi.org/10.1016/j.compbiomed.2025.110841
Received 2 January 2025; Received in revised form 10 July 2025; Accepted 21 July 2025
Available online 25 July 2025

near-real-time analysis of rapidly frozen and stained histopathological sections. Traditionally, as noted in Ref. [8], computational pathology has relied on RGB images of these sections, which limits information to the visual range and excludes the data across the continuous spectral range. To address this limitation, hyperspectral imaging (HSI) technology is increasingly being used in various medical imaging applications, including computational pathology. We refer interested readers to Ref. [8] for an overview of computational pathology from 2013 to 2019, to Ref. [9] for surgical applications over the same period, to Ref. [10] for medical HSI research from 1998 to early 2013, and to Ref. [11] for the review of major developments of spectral imaging technology in the biomedical field.

Although HSI has demonstrated its potential to detect diseases-related pathological changes, several unresolved issues still prevent the routine use of HSI in computational pathology. While HSI is generally assumed to offer performance improvements over RGB imaging, the number of studies supported this claim is limited, as highlighted in Ref. [8], and further research is needed to confirm the advantages of HSI technology over traditional RGB images. Studies such as [12–15] are addressing this gap. Since HSI captures both spatial (morphological) and spectral information from specimens, classifiers that leverage both spectral and spatial features have been shown to outperform those relying solely on spectral information [3,7,13,15–23]. Most of the architectures cited above are deep networks, which require large amounts of annotated HSI data for training to avoid overfitting. However, as noted in Refs. [8,14,24,25], there is a significant lack of annotated HSI databases. That is especially the case with the HSI databases in histopathology annotated on pixel level and that is required for solving tumor demarcation problem. Two primary factors contribute to this shortage. First, due to time constraints, data collection during intraoperative procedures is demanding, even for RGB microscopic images [1]. Second, pixel-wise annotation requires pathologists, whose availability is limited. Additionally, the appearance of HSI data differs significantly from RGB images, making the annotation process even more challenging [13]. Our investigation on HSI databases in histopathology discovered that only [14,25] provide ground truth information based on pixel-wise labeling by pathologists. Outlined factors hinder the routine usage of HSI in computational pathology. To address this, several HSI databases have been created [19,22,26–28]. However, due to the privacy protection reason public access to HSI databases in histopathology is allowed only in Refs. [14,25–28].

Motivated by the issues outlined above we present herein the following contributions:

1) HSI database creation: We introduce a novel database of 27 HSIs of hematoxylin-eosin (H&E) stained frozen sections, collected intraoperatively from 14 patients with colon adenocarcinoma metastasized to the liver. The HSIs were acquired in spectral range from 450 nm to 800 nm, with a 1 nm resolution. To the best of our knowledge, a HSI database for specified diagnosis does not exist yet, at least not with public access. In addition to the HSIs, the dataset includes pixel-wise ground truth maps labeled by three pathologists, distinguishing cancerous and non-cancerous pixels, as well as co-registered pseudo RGB images. The ground truth maps are accompanied with rigorous kappa-statistics-based assessment of inter- and intra-annotator agreement. To the best of our knowledge, this is the first HSI dataset of frozen sections for this metastatic colon cancer in the liver, addressing the scarcity of intraoperative HSI datasets, particularly for metastatic colorectal cancer.
2) A Grassmann manifold and nearest subspace classifier approach to semi-supervised learning with spectral-spatial features: To address challenges such as costly expert labeling, experimental variability, and limited annotated data, we propose combination of Grassmann manifold [29,30] and nearest subspace classifier for pixel-wise classification of HSIs. We estimate Grassmann points, bases of subspaces that represent cancer and non-cancers classes, from small neighborhoods of randomly selected small percentage of labeled pixels. Labels are assigned to the rest of the pixels by using the nearest subspace classifier. In combination with Grassmann manifold approach, we leverage recently developed spectra-spatial feature extraction technique called tensor singular spectrum analysis (TensorSSA) [31]. We compared proposed approach with label-propagation-based semi-supervised learning method achieving high-quality classification performance with as little as 0.5 % of labeled pixels. Unlike deep networks, proposed approach can be applied on a HSI-by-HSI basis, making it suitable for very few HSIs. Proposed methodology is illustrated in Fig. 1.

2. Materials and methods

Hyperspectral imaging technology has been widely used for many years in remote sensing, supporting applications in resource management, agriculture, exploration of minerals, monitoring of environment, and more [32]. Since the late 1990s, HSI has also been applied in various medical imaging applications, showing significant potential in cancer diagnosis for the cervix, breast, colon, head and neck, prostate, ovary and lymph nodes, among others. For more detailed references on these applications see Ref. [10].

2.1. Hyperspectral imaging in computational pathology

In this section, we provide review of HSI databases in histopathology. Since our contribution is focused on tumor demarcation, we focus on databases that satisfy the following criteria: (*i*) annotation is performed on pixel-wise level; (*ii*) co-registered RGB or pseudo RGB images are available together with HSIs; (*iii*) HSIs are recorded at the high spectral resolution (*iv*) database is public. A hyperspectral microscopic pathological dataset of cholangiocarcinoma is presented in Ref. [14]. Dataset contains 880 hyperspectral images collected from 174 patients with pixel-wise tumor labeling by pathologists. HSIs are acquired in spectral range between 500 nm and 1000 nm at 30 spectral channels. Binary prediction of convolutional neural network (CNN) on the patch level is combined with random forest classifier for prediction on the scene (image) level and that achieved accuracy of 0.937. Dataset is publicly available. Performance improvement in comparison with RGB images is demonstrated as well. A large-scale dataset is built containing HSIs of 924 scenes of precancerous lesions in gastric cancer [15]. HSIs were acquired in spectral range between 450 nm and 700 nm at 40 spectral channels, i.e. 6.25 nm spectral resolution. Self-supervised learning method is developed and applied in combination with pre-trained ResNet18 and ResNet50 backbones. The method is focused on diagnosis on the patch level in terms of normal, intestinal metaplasia and gastric intraephitelial neoplasia. Performance improvement in comparison with RGB images is demonstrated as well. Dataset is not publicly available. A dataset containing 469 HSIs of 13 patients diagnosed with glioblastoma is presented in Ref. [24]. HSIs were acquired in spectral range between 400 nm and 1000 nm at 826 spectral channels. Pathologists provided annotations on the image level. Dataset is publicly available. A multidimensional publicly available Choledoc database is described in Ref. [25]. It contains HSIs and RGB images of 880 scenes of 174 patients diagnosed with cholangiocarcinoma with the pixel-wise annotations of the tumor cells. HSIs were acquired in spectral range between 550 nm and 1000 nm at 60 spectral channels. A publicly available dataset containing 517 HSIs of brain tissue with glioblastoma is presented in Ref. [28]. HSIs were acquired in spectral range between 400 nm and 1000 nm with a resolution of 2.8 nm, i.e. 826 spectral channels. Samples were extracted during brain tumor surgery and stained with H&E. Images are annotated on the regions-of-interest level. A database containing HSIs from 68 patients with two types of membranous nephropathy (MN) is introduced in Ref. [27]. A tensor patch-based linear discriminative regression method was proposed for classification, exploiting the characteristics of medical HSIs. In

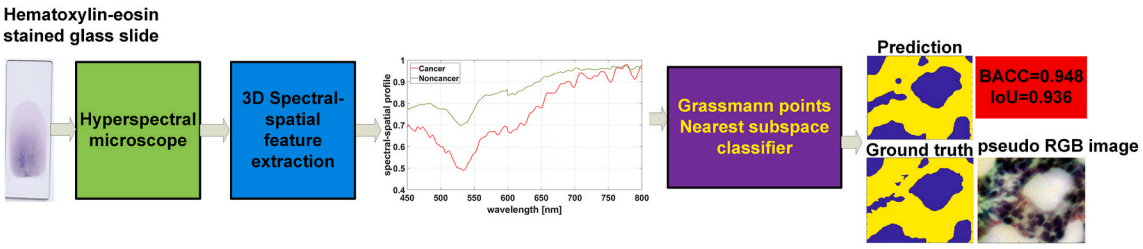

Fig. 1. Illustration of the proposed Grassmann manifold approach for semi-supervised pixel-wise classification of hyperspectral images (HSIs) of frozen sections from metastatic colon cancer in the liver. Using TensorSSA spectral-spatial features [31], Grassmann manifold approach outperforms significantly a label-propagation based semi-supervised learning approach to pixel-wise classification of HSIs, see section 3.4. Yellow color indicates cancerous tissue and blue color represents non-cancerous tissue. (For interpretation of the references to color in this figure legend, the reader is referred to the Web version of this article.)

Ref. [33], a key challenge in surgical HSI is addressed - the development of public intraoperative HSI neurosurgical database. The HSI camera captures images within the 500 nm–900 nm spectral range, and a spectral resolution of 3 nm–5 nm. Corresponding RGB images were also obtained as anatomical references, which were used to label the HSI data. The database includes 52 HSIs acquired during 10 microsurgical operations. In Ref. [34], the use of HSI acquired over micro-FTIR HSI absorbance spectroscopy for characterizing of cancerous, inflammatory and healthy colon tissues is discussed. In total 71 HSIs were acquired: 24 form healthy tissue, 27 from inflammatory tissue and 20 from cancerous tissue. In comparison with discussed datasets, our dataset is the only one containing HSI of metastatic colon cancer in the liver. It is also among the few datasets only that are publicly available. In addition to our dataset, only two more datasets are annotated on the pixel level, i.e. they can be used for studies related to tumor demarcation. Our dataset is recorded at the spectral resolution of 1 nm which also makes it unique.

2.2. Hyperspectral image database

The database consists of 27 HSIs of H&E stained frozen sections, collected intraoperatively from 14 patients diagnosed with adenocarcinoma of the colon in the liver. These specimens were gathered through a clinical study funded by the Croatian science foundation grant IP-2016-06-5235, conducted between March 2017 and February 2020 at the Department of Pathology and Cytology, Clinical Hospital Dubrava, Zagreb, Croatia. The Institutional Review Board of Clinical Hospital Dubrava approved the collection of samples on May 24, 2016. All patients provided written informed consent, and the data were anonymized. The HSIs were recorded across a spectral range of 450 nm–800 nm, with a spectral resolution of 1 nm, and a spatial resolution of 0.11 μm^2. Each image has a size of 1384 × 1035 pixels and is stored in HDF5 format. Accompanying each HSI is a binary ground truth map created through majority voting of pixel-wise annotations by two pathologists (A.P and M.M.P) and a medical expert (M.H). Two images per patient were acquired for thirteen patients and one image for one patient. Regarding the cancer stages, for twelve patients they are given as pT4aN2aM1a, pT2N1aM1a, pT3N2aM1a, pT3N0M1a, pT3N0M1a, pT3N0M1a, pT3N2bM1a, pT1N0M1a, pT3N4aM1a, pT3(2)N1bM1a, pT4aN1aM1a and pT3N2bM1a. For two patients staging information is not available.

2.2.1. Hyperspectral image acquisition

Regions of interest were marked by pathologists on H&E stained histopathological specimens. These regions were then imaged using Photon etc's hyperspectral fluorescence microscope IMA, [35], as shown in Fig. 2. The IMA employs volume Bragg gratings (VBG) to capture spectrally resolved images, which are combined into a hyperspectral data cube. The use of VBG allows for global imaging, where signals from all points within the field of view are collected simultaneously, avoiding the need for x-y or line scanning. The resulting data cubes are composed of 351 Gy scale images, each with a spectral resolution of 1 nm, covering the 450 nm–800 nm range, with a focus at 590 nm. Broadband source was used for illumination. The images were captured using a 20 × objective lens with the exposure time of 500 ms, producing images of 1392 × 1040 pixels with a field-of-view of 449μm × 335 μm. This corresponds to a spatial resolution of 0.11 μm^2 per pixel, which effectively eliminates the mixing of cancer and non-cancer tissues at the pixel level. To avoid edge effects, we retained rows 4:1387 and columns 6:1040 columns, resulting in a final data cube size of 1384 × 1035 × 351. Data were normalized using the lamp spectrum. Fig. 3 shows spatially averaged spectral profiles of one pixel labeled as cancerous and another labeled as non-cancerous.

2.2.2. Pixel-wise annotation

Pixel-wise annotation was performed by two pathologists, (A.P. and M.M.P.), and one medical expert (M.H.). Pixel-wise labeling of HSIs is challenging for pathologists due to the visual differences between HSIs and RGB images [13]. Since HSI system used in Fig. 2 cannot capture co-registered HSIs and RGB images simultaneously, we adopted the approach from Ref. [19]. For each HSI, we constructed a corresponding pseudo RGB image, a common practice in remote sensing for HSI visualization [36].[3] This process involves generating realistic color images by mapping the visible spectrum of the HSIs to the CIE XYZ color space, then converting it to the standardized RGB color space. Subsequently, pixel-wise labeling by experts was conducted on pseudo RGB images, aided by a super-pixels-based software system, described in Ref. [1]. Fig. 4 shows an example of pseudo RGB image constructed from a HSI, along with its ground truth map, generated by majority voting as explained below.

The annotation process is inherently affected by inter-observer and intra-observer variability, which can introduce subjectivity into the labeling of images [37]. To address this issue, three experts are involved in the annotation process. After an initial round of annotations on pseudo RGB images, the same three experts were asked to repeat the annotation process three months later. To evaluate the reliability of the annotations and measure agreement among the annotators, Fleiss' kappa statistics were employed [38,39]. Table 1 presents kappa statistics intra-annotator agreements reproduced from Ref. [38]. Table 2 presents the estimated kappa values indicating the agreement among three annotators (two pathologists and one medical expert) for the first and second labeling sessions. According to Table 1, the agreement between the two pathologists was nearly perfect in both annotations, while their agreement with medical expert was significantly lower, particularly during the first annotation.

It can be observed from Table 2, that the agreement between medical expert (M.H.) and the two pathologists improved in the second annotation session. For the formation of the final ground truth, we utilized both annotations from the pathologists and the second annotation from

[3] The MATLAB code for method from Magnusson et al. (2020) https://github.com/JakobSig/HSI2RGB.

Fig. 2. Hyperspectral fluorescence microscopy system equipped with volume Bragg gratings and an optical microscope.

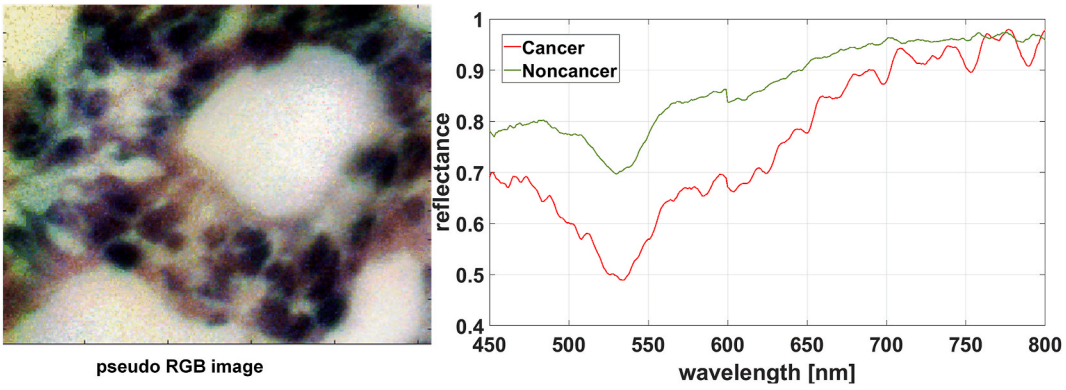

Fig. 3. Left: Pseudo RGB image of a patch from which cancerous and non-cancerous pixels were extracted. Right: Spatially averaged spectra of cancer-annotated pixel (red) and non-cancer-annotated pixel (green) in the 450–800 nm range, with a spectral resolution of 1 nm. Spectra are averaged on neighborhood with the size of 5 × 5 pixels. (For interpretation of the references to color in this figure legend, the reader is referred to the Web version of this article.)

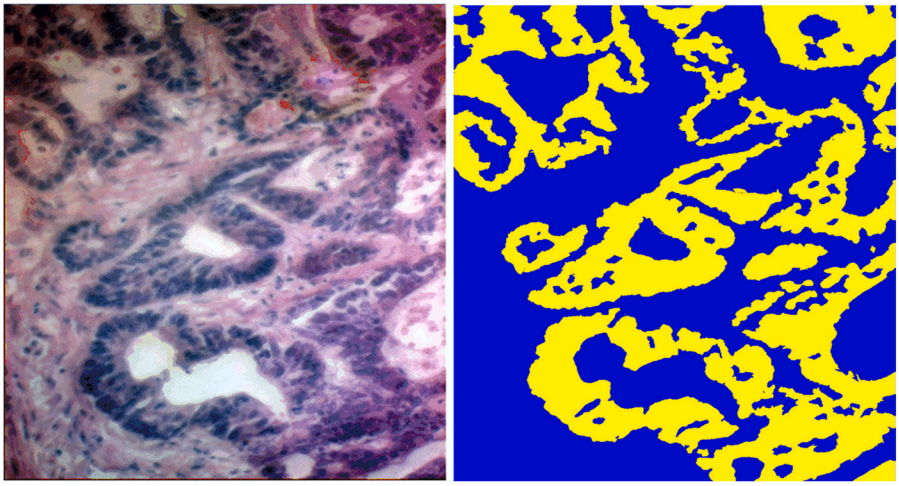

Fig. 4. Pseudo RGB image (left) constructed from the corresponding HSI using the method from Ref. [36]. The associated ground truth map (right) shows pixel-wise annotations, where yellow color indicates cancerous tissue and blue color represents non-cancerous tissue. (For interpretation of the references to color in this figure legend, the reader is referred to the Web version of this article.)

Table 1
Kappa statistics and strength of agreement [38].

Kappa statistics	Strength of Agreement
<0.00	Poor
0.00–0.20	Slight
0.21–0.40	Fair
0.41–0.60	Moderate
0.61–0.80	Substantial
0.81–1.00	Almost Perfect

Table 2
Inter-annotators agreements in terms of kappa statistics for two annotation sessions. 0.61≤kappa≤0.8 indicates substantial agreement, see Table 1.

Annotation	AP-MMP-MH	AP-MMP	AP-MH	MMP-MH
1.	0.6966	0.7698	0.6542	0.6636
2.	0.7228	0.7687	0.6827	0.7136

the medical expert through majority voting. The estimated kappa statistics for selected five annotations was $\kappa = 0.754$ which, according to Table 1, indicates the substantial agreement. To contribute further to the transparency of the annotation process we show in Fig. 5 kappa statistics estimated between "five" annotators on image-by-images basis. It can be observed that agreement on only one image is below substantial as well as that agreements on six images are almost perfect.

Fig. 6 displays the annotations made by the two pathologists and the medical expert for the pseudo RGB image shown in Fig. 4. The source of disagreement between the pathologists and the medical expert stemmed from the categorization of a necrotic area within the tumor, which was addressed and resolved in the second annotation.

2.3. Methodology

As indicating in the Introduction, in addition to hyperspectral image database another contribution of the paper is a Grassmann manifold and nearest subspace classifier approach to semi-supervised pixel-wise classification of hyperspectral images. This is motivated by need to reduce the reliance on a large amount of annotated pixels for training as well as by need to cope with batch effects caused by experimental variabilities.

2.3.1. Grassmann manifold approach to semi-supervised pixel-wise classification of HSIs

Pixel-wise classification of HSIs can be seen as instance of wider problem related to clustering high-dimensional data with complex intrinsic relations and nonlinear manifold structure. This problem is known as demanding [28], and it is dominantly addressed by kernel-based methods and deep networks-based methods. However, the Grassmann manifold-based representation is legitimate candidate to address this problem, see Refs. [40–43] for examples of Grassmann manifold approaches to clustering data from nonlinear manifolds. Let us assume the HSI cube is represented as $\mathscr{X} \in \mathbb{R}^{h\times w\times b}$, where h represents number of rows, w represents number of columns and b represents number of spectral bands. The canonical Union-of-Subspaces (UoS) model asserts that data in a b-dimensional ambient space can be represented through a union of C low-dimensional subspaces [44,45]: $\mathscr{M}_C = \cup_{c=1}^{C}\mathscr{S}_c$, Σ_c is a subspace in $\mathbb{R}^b$. Thereby, $\dim(\Sigma_c) = d_c \ll b$. By assuming further $\{d_c = d\}_{c=1}^{C}$, each Σ_c corresponds to a point on the Grassmann manifold $\mathscr{G}(b,d)$, which denotes the set of all d-dimensional linear subspaces of b-dimensional Euclidean spaces [30] [4]:

$$\mathscr{G}(b,d) = \left\{\mathbf{Y} \in \mathbb{R}^{b\times d} : \mathbf{Y}^{\mathrm{T}}\mathbf{Y} = \mathbf{I}_d\right\} / \mathscr{O}(d) \tag{1}$$

where $\mathscr{O}(d)$ represents the group of d-orthonormal matrices and $d \le b$. Each point on $\mathscr{G}(b,d)$ is represented as follows:

$$\mathscr{S} := \mathrm{span}_d(\mathbf{Y}) \tag{2}$$

Equation (1) ensures the equivalence relation:

$$[\mathbf{Y}] = \left\{\mathbf{YQ} \middle| \mathbf{Y}^{\mathrm{T}}\mathbf{Y} = \mathbf{I}_d, \mathbf{Q} \in \mathscr{O}(d)\right\}. \tag{3}$$

Two representatives $\mathbf{Y}_1$ and $\mathbf{Y}_2$ are equivalent if there exists $\mathbf{Q} \in \mathscr{O}(d)$ such that $\mathbf{Y}_1 = \mathbf{Y}_2\mathbf{Q}$. In other words, the two representatives $\mathbf{Y}_1$ and $\mathbf{Y}_2$ are equivalent if they span the same subspace:

$$\mathrm{span}_d(\mathbf{Y}_1) = \mathrm{span}_d(\mathbf{Y}_2). \tag{4}$$

Therefore, usually one representative is taken to represent the Grassmann point. In pixel-wise classification problem considered in the paper, the HSI tensor Ξ is matricized:

$$\mathscr{X} \in \mathbb{R}^{h\times w\times b} \rightarrow \mathbf{X} \in \mathbb{R}^{b\times hw} \tag{5}$$

It is clear that proposed Grassmann manifold approach is derived for multiclass problem. However, since the current paper is focused on tumor demarcation problem we assume the existence of two classes or groups: cancerous and non-cancerous, i.e., $C = 2$. Thus, the pixels labels are from the set $\{c_i \in \{0,1\}\}_{i=1}^{hw}$. By convetion 0 implies non-cancerous pixels and 1 implies cancerous pixels. To estimate representatives of the Grassmann points, $\mathbf{Y}_0$ and $\mathbf{Y}_1$, on non-canerous and cancerous manifolds we need to form non-cancerous and cancerous pixel-sets $\left\{\breve{\mathbf{X}}_c \in \mathbb{R}_{0+}^{b\times \breve{n}_c}\right\}_{c\in\{0,1\}}$ from which representatives of Grassmann points will be estimated according to:

$$\begin{aligned} &\breve{\mathbf{X}}_c = \mathbf{U}_c\mathbf{\Sigma}_c\mathbf{V}_c^{\mathrm{T}} \\ &\mathbf{Y}_c \in \mathbb{R}^{b\times d} = \mathbf{U}_c(:,1:d) \quad c \in \{0,1\} \end{aligned} \tag{6}$$

where d in (6) represents the uknown subspace dimension. In the spirit of semi-supervised learning (SSL), [46,47], we select a small amnout of labeled data, $\left\{\breve{\mathbf{X}}_{cc}\right\}_{c=0}^{1}$, from each category. Then, according to (6) we construct representatives of Grassmann points, $\mathbf{Y}_0$ and $\mathbf{Y}_1$, that correspond to non-cancerous and cancerous category. Classification of the remaning pixels belonging to the set $\breve{\mathbf{X}} \in \mathbb{R}_{0+}^{b\times n_x} := \mathbf{X}\backslash\left\{\breve{\mathbf{X}}_0 \cup \breve{\mathbf{X}}_1\right\}$ is based on the minimum of a point-to-subspace distance criterion [48]. For this purpose we first compute:

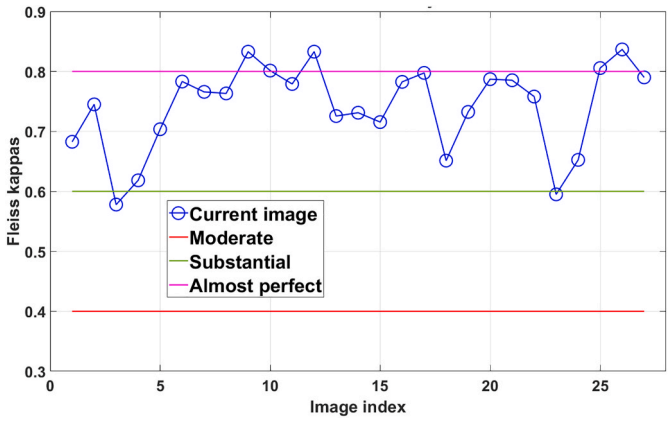

Fig. 5. Kappa statistics estimated between "five" annotators on image-by-image basis.

[4] From $\dim(\Sigma_c) = d_c \ll b$ it is evident that, due to low-dimensionality of the ambient space, the Grassmann manifold concept is not applicable to pixel-wise classification of RGB images where $b = 3$.

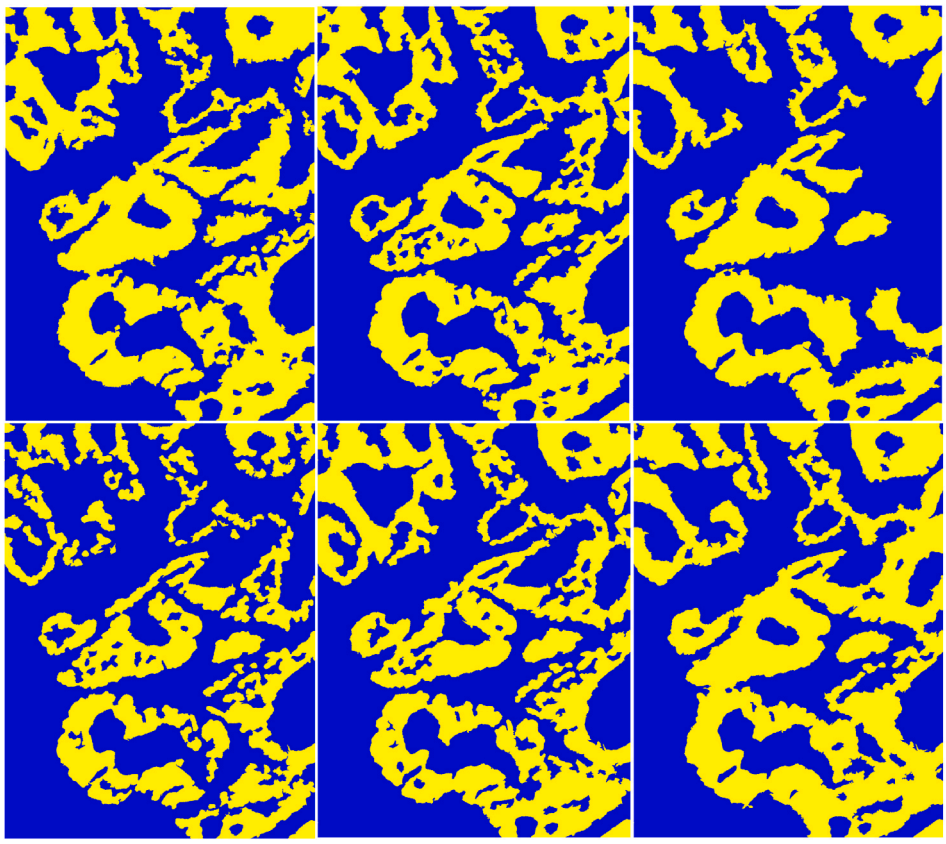

Fig. 6. Annotations from two pathologists and one medical expert are presented from left to right. Each set of annotations is shown from top to bottom: the first annotation followed by the second annotation. Yellow color indicates pixels annotated as cancer, and blue color indicates pixels annotated as non-cancer. (For interpretation of the references to color in this figure legend, the reader is referred to the Web version of this article.)

$$\left\{ \breve{\mathbf{X}}_c \leftarrow \breve{\mathbf{X}}_c - \left[\underbrace{\boldsymbol{\mu}_c \cdots \boldsymbol{\mu}_c}_{\breve{n}_c \text{ times}} \right] \right\} \quad c \in \{0,1\} \tag{7}$$

where:

$$\boldsymbol{\mu}_c = \frac{1}{\breve{n}_c} \sum_{i=1}^{\breve{n}_c} \mathbf{X}_c(:,i) \quad c \in \{0,1\}. \tag{8}$$

We now apply (6) to $\left\{\breve{\mathbf{X}}_c\right\}_{c=0}^{1}$ to estimate representatives $\{\mathbf{Y}_c\}_{c=0}^{1}$. Note that despite (7) and (8), $\{\mathbf{Y}_c\}_{c=0}^{1}$ are still representatives of Grassmann points because they satisfy condition (1): $\mathbf{Y}_c^{\mathrm{T}}\mathbf{Y}_c = \mathbf{I}_d \;\; c \in \{0,1\}$. We now assign label to a new pixel $\mathbf{x} \in \breve{\mathbf{X}}$ according to Ref. [26]:

$$l(\mathbf{x}) = \underset{k\in\{0,1\}}{\operatorname{argmin}} \; \left\| \tilde{\mathbf{x}}^k - \mathbf{Y}_k \mathbf{Y}_k^{\mathrm{T}} \tilde{\mathbf{x}}^k \right\|_2 \tag{9}$$

where $\tilde{\mathbf{x}}^k = \mathbf{x} - \boldsymbol{\mu}_k$. We summarize our approach to pixel-wise classification on Grassmann manifolds in Algorithm 1.

Algorithm 1. Pixel-wise classification on Grassmann manifolds

Input: Vectorized hyperspectral image $\mathbf{X} \in \mathbb{R}_{0+}^{b\times hw}$. Labeled pixel-subsets $\breve{\mathbf{X}}_c \in \mathbb{R}^{b\times \breve{n}_c}$ $c \in \{0,1\}$. We assume $\breve{n}_0 = \breve{n}_1 = n$.

Step 1: Compute $\breve{\mathbf{X}}_c \leftarrow \breve{\mathbf{X}}_c$ $c \in \{0,1\}$ using (7) and (8).

Step 2: Compute representatives $\mathbf{Y}_0$ and $\mathbf{Y}_1$ of Grassmann points using (6).

Step 3: Assign label l(**x**) to arbitrary pixel $\mathbf{x} \in \breve{\mathbf{X}} := \mathbf{X} \backslash \left\{ \breve{\mathbf{X}}_0 \cup \breve{\mathbf{X}}_1 \right\}$ using (9).

Output: Assigned labels l(**x**): $\mathbf{x} \in \breve{\mathbf{X}} := \mathbf{X} \backslash \left\{ \breve{\mathbf{X}}_0 \cup \breve{\mathbf{X}}_1 \right\}$.

To improve quality of classifier as well as quality of representatitvness in the Algorithm 1 we can apply spatial averaging by taking into account the local neighborhood information. To be specific we define the neighborhood around selected pixel:

$$\mathbf{x}_{ij} \in \mathbb{R}_{0+}^{b} = \mathscr{X}(i,j,:) \quad i \in \{1,\ldots,h\}, j \in \{1,\ldots,w\}.$$

We form a local patch:

$$\mathscr{X}_{ij} \in \mathbb{R}_{0+}^{(2p+1)\times(2p+1)\times b} \quad p \in \mathbb{N}_0 \tag{10}$$

centered at $\mathbf{x}_{ij}$. If $p = 0$, the local patch $\mathscr{X}_{ij}$ coincides with $\mathbf{x}_{ij}$. The total number of pixels in the patch is $(2p+1)^2$. We assume that in the local neighborhood of $\mathbf{x}_{ij}$ are mostly the pixels belonging to the same category (cancerous or non-cancerous). Thus, it is important that p is not too large. In the experiments reported in section 3.4 we used $p \in \{0, 1, 2, 3, 4, 5, 6, 7\}$ and achieved the best results with $p = 5$. Now, we map $\mathbf{x}_{ij}$ into the patch mean (spatial average):

$$\mathbf{x}_{ij} \rightarrow \overline{\mathbf{x}}_{ij}$$

$$\overline{\mathbf{x}}_{ij} = \frac{1}{(2p+1)^2} \sum_{k=1}^{2p+1} \sum_{l=1}^{2p+1} \mathscr{X}_{ij}(k,l,:) \tag{11}$$

We perform mapping (11) in both cases, when computing the representatives of Grassmann points from labeled pixel subsets, as well as when assigning labels to arbitrary pixels from $\breve{\mathbf{X}}$.

2.3.2. HSI classifiers based on spectral-spatial features

As is discussed in Section 2.1, designing a deep architecture that effectively extracts discriminative spectral-spatial features from HSIs while reducing the need for a large amount of annotated pixels for training is challenging. As noted in Ref. [9], it is also crucial that the proposed architecture demonstrates a significant improvement in classification performance using HSIs compared to RGB images. These challenges are consistent with the experience in the remote sensing community, where deep-network-based HSI classification methods either offer only marginal improvements over hand-crafted features or require significantly more labeled data [49].

2.3.2.1. The SSL classifier. The SSL approach [46] is motivated by need to reduce the reliance on a large amount of annotated pixels for training. SSL algorithms aim to train a classifier and assign labels to unlabeled data, starting with a classifier trained on a small labeled dataset. Specifically, we used a self-training SSL algorithm [47], which assigns pseudo-labels to high-confidence unlabeled samples. These samples are then added to the training set, and the classifier is iteratively improved. In our implementation of this SSL classifier, we utilized the MATLAB function `fitsemiself`.

2.3.2.2. The TensorSSA spectral-spatial features. Tensor Singular Spectrum Analysis (TensorSSA) [31],[5] is designed to extract global and low-rank 3D spectral-spatial features from HSI. The low-rank nature of extracted features is guaranteed through the tensor singular value decomposition (t-SVD) model [50]. The TensorSSA method first performs adaptive embedding of the HSI $\mathscr{X} \in \mathbb{R}^{h\times w\times b}$ onto a tensor $\mathscr{Z} \in \mathbb{R}^{l\times hw\times b}$, where $n \times n$ is the size of the patch centered around each pixel, with n=2u+1. $l \leq (n\text{-}2)^2$ is the number of pixels surrounding the central pixel that are evaluated for similarity to the central pixel, based on the normalized Euclidean distance. Both u and l are hyperparameters of the TensorSSA method. In our experiments reported in Section 3, after cross-validation we set u=5 and $l = 8$ for processing pseudo RGB images, and $u = 5$ and l=60 for processing HSIs. The trajectory tensor $\mathscr{Z}$ contains both spectral and spatial information corresponding to the entire HSI. The tensor $\mathscr{Z}$ is then replaced by its t-SVD-based low-tensor-tubal-rank approximation, i.e., $\mathscr{Z} \rightarrow \mathscr{Z}_{rtub} \in \mathbb{R}^{l\times hw\times b}$, where tubal rank satisfies $rtub \ll \min(l, hw)$. Experiments carried out in Ref. [31] showed that $rtub = 1$ works well. The tensor $\mathscr{Z}_{rtub}$ is subsequently re-projected to $\mathscr{Y} \in \mathbb{R}^{h\times w\times b}$, which contains 3D spectral-spatial features associated with Ξ. While in Ref. [31] a linear support vector machine (SVM) algorithm was used to classify HSI based on these spectral-spatial features $\mathscr{Y}$, in this paper, we employ Grassmann manifold SSL classifier and label-propagation SSL classifier.

2.3.2.3. The MPRI spectral-spatial features. The multiscale principle of relevant information (MPRI) architecture was recently introduced in hyperspectral remote sensing [51]. It learns discriminative spectral-spatial features for HSI classification by leveraging PRI [52]. For a random variable $\mathbf{X}$ with a known probability density function (PDF) g, PRI aims to learn a reduced statistical representation of $\mathbf{X}$, instantiated in a random variable $\mathbf{Y}$ with PDF f. This is framed as trade-off between the entropy $H(f)$ of $\mathbf{Y}$ and its descriptive power regarding $\mathbf{X}$, quantified by the divergence $D(f||g)$ [51,52]:

$$\min_f H(f) + \beta D(f\|g). \tag{12}$$

Here, β is a hyper-parameter that controls the amount of relevant information $\mathbf{Y}$ that can be extracted from $\mathbf{X}$. The PRI optimization problem from (12) is then formulated as [51]:

$$f_{opt} \equiv \operatorname*{argmin}_f (1-\beta)H_2(f) + 2\beta H_2(f;g) \tag{13}$$

where $H_2()$ represents Reny's 2-entropy. Let us assume $\mathbf{X} := \{\mathbf{x}_i\}_{i=1}^N$ and $\mathbf{Y} := \{\mathbf{y}_i\}_{i=1}^N$ are realizations of random variables drawn independently from g and f, respectively. Using a Parzen's window-density estimator with a Gaussian kernel $G_\sigma(\cdot) = \exp(-\|\cdot\|^2/2\sigma^2)$ [53], equation (2) can be written as [54]:

$$\mathbf{Y}_* = \operatorname*{argmin}_{\mathbf{Y}} \begin{bmatrix} -(1-\beta)\log\left(\frac{1}{N^2}\sum_{i,j=1}^{N} G_\sigma(\mathbf{y}_i - \mathbf{y}_j)\right) \\ -2\beta\log\left(\frac{1}{N^2}\sum_{i,j=1}^{N} G_\sigma(\mathbf{y}_i - \mathbf{x}_j)\right) \end{bmatrix}. \tag{14}$$

Now, let us assume the HSI is given as a 3D data cube $\mathscr{X} \in \mathbb{R}^{h\times w\times b}$. Around each target vector $\mathbf{t}_* \in \mathbb{R}^b$, a local patch $\mathbf{T} \in \mathbb{R}^{N\times b}$ is extracted using a sliding window of size n, centered at $\mathbf{t}_*$. The total number of pixels in the patch is $N = n \times n$, and $\mathbf{t}_* = \mathbf{T}_{\lfloor n/2+1, \lfloor n/2+1}$, where $\lfloor \cdot$ denotes the nearest integer function. The PRI-based spectral-spatial characterization $\mathbf{Y}_* \in \mathbb{R}^{N\times b}$ of $\mathbf{T}$ is then computed using equation (14), making the estimation fully data driven. The PRI-based representation for the current patch is given by $\mathbf{t}_* = \mathbf{Y}_{\lfloor n/2+1, \lfloor n/2+1}$, and scanning the entire 3D cube $\mathscr{X}$ yields the PRI-based spectral-spatial representation $\mathscr{Y} \in \mathbb{R}^{h\times w\times b}$. To obtain PRI at multiple scales, procedure can be repeated for patches of varying sizes n, resulting in a multiscale PRI. The patch-size n is a hyperparameter. To reduce feature redundancy, regularized linear discriminant analysis is applied [51,55]. A multilayer structure is created by feeding PRI-based spectral-spatial features from one layer into the input of the next. The final spectral-spatial representation is obtained by concatenating the representations from each layer. In the original work [51], this representation is used with a standard k-nearest neighbor (k-NN) classifier. In our contribution, we use Grassmann manifold-based SSL classifier and label propagation-based SSL classifier, as they achieve comparable performance with significantly less labeled samples. The MPRI architecture has four hyper-parameters that need tuning during cross-validation: the number of scales (determined by the patch size n), β, the number of layers, and the kernel variance σ^2 [51]. In our implementation,[6] after cross-validation, we selected three layers, $n \in \{3, 7, 11\}$, $\beta \in \{2, 3\}$ and $\sigma^2 = 0.3$. Consequently, the MPRI architecture transforms a spectral pixel vector into 6D spectral-spatial feature vector. This was used in combination with the label propagation SSL classifier. Grassmann manifold based SSL classifier demands that subspace dimension d is less than or equal to the ambient space dimension. Therefore, this approach is not applicable to features with reduced dimensionality. Instead, we applied Grassmann manifold approach to concatenated feature vectors of multiscale MPRI, i.e., we combined raw features from three scales and two values of β. That yields 6 × 351 feature vector with a cross-validate subspace dimension $d = 50$.

2.3.2.4. Deep learning HSI classifiers. As discussed in Section 2.1, significant efforts have been made to design architectures that can effectively extract spectral-spatial features from HSIs, while reducing the need for large amount of annotated pixels for training. Several specialized architectures, such as S^3-R in Ref. [13] and HyperNet [56] have been proposed for this purpose. These architectures address the limited ability of U-shaped networks to model long-range contextual relationship across the spectral dimension of HSIs [13,56]. One such network termed U-within-U-Net (UwU-Net),[7] was introduced in Ref. [57] as a

[5] The MATLAB code for TensorSSA method is available at: https://github.com/RsAI-lab/TensorSSA.

[6] The initial MATLAB-based implementation of MPRI is available at: http://bit.ly/MPRI_HSI.

[7] The code for UwU-Net is available at https://doi.org/10.5281/zenodo.4396327.

convolutional framework that preserves spatial resolution and accommodates an arbitrary number of spectral channels. In Section 3, we apply UwU-Net to the segmentation of HSIs and pseudo RGB images of adenocarcinoma of the colon in the liver. Another network, nnUnet, was proposed in Ref. [58], with code in Supplementary Software link, to address the limitations of existing deep-learning-based methods for segmenting biomedical datasets. nnUnet automatically configures itself for a new segmentation task, and since it was trained on a large and diverse data pool, it is expected to perform well on datasets with limited training data. Therefore, we also applied nnUnet to the segmentation HSIs and pseudo RGB images of adenocarcinoma of the colon in the liver. Additionally, to corroborate some previous findings, we applied well-known deep networks for the classification of both HSIs and corresponding pseudo RGB images: DeepLabv3+ [59], Unet [60], Unet++ [61], and MA-Net [62]. MA-Net, in particular, incorporates a self-attention mechanism and is expected to effectively capture both spatial and spectral feature dependencies.

3. Results

We conducted experiments to validate whether: (*i*) proposed Grassmann manifold based semi-supervised classification method yields the highest classification performance in comparison with some state-of-the-art methods; (*ii*) selected state-of-the-art methods provide significantly better classification of cancerous and non-cancerous pixels from HSIs compared to corresponding pseudo RGB images (in terms of statistical significance), and (*iii*) proposed semi-supervised classification methods can reduce the need for a large number of labeled pixels necessary for training.

3.1. Software environment

We implemented the Grassmann manifold-TensorSSA and -MPRI classifiers, the SSL-MPRI, SSL-TensorSSA classifiers, k-NN-MPRI and SVM-TensorSSA classifiers in MATLAB on a computer running a 64-bit Windows 10 operating system. The computer was equipped with 256 GB of RAM and an Intel Xeon CPU E5-2650 v4 2 processor, operating at a clock speed of 2.2 GHz. All deep learning-based classifiers were implemented using the PyThorch software environment [63].

3.2. Train and test protocols

3.2.1. The Grassmann manifold-, SSL-, k-NN- and SVM classifiers combined with MPRI and TensorSSA 3D spectral-spatial features

Due to the memory constraints, the Grasmmann manifold semi-supervised classifier combined with MPRI and TensorSSA features, label-propagation SSL-MPRI and SSL-TensorSSA classifiers, k-NN and SVM classifiers operated on input patches of size 230 × 258 pixels, i.e. each HSI was split into 24 non-overlapping patches. As a result, these classifiers work on a patch-by-patch basis, allowing them to handle cases where only a single image is available in a given scenario. This approach is often applied in deep learning models from remotely sensed HSIs [49].

3.2.2. Deep learning classifiers

For the deep learning classifiers, we split the datasets, consisting of both HSIs and pseudo RGB images into 63 % for training (17 images) and 37 % for testing (10 images). To ensure fair performance validation, we made sure that the test set images came from different patients than the training set. In other words, the test set included five patients, none of whom was part of the training set, which contained images from nine patients. Regarding the deep networks used in the experiment (Unet, Unet++, DeepLabv3+, MA-Net, nnUnet, and UwU-Net) pixel values were normalized to a range between 0 and 1. We also applied a patching process using a 128 × 128 window with strides of 64 pixels. Additionally, 20 % of the preprocessed train set was set aside as a validation set. We trained each deep network model ten times from the scratch always with the same partition. Our aim was to verify robustness of the models to the variations of the initial conditions.

3.3. Performance measures

We used six metrics to evaluate classification performance of different architectures on HSIs and their corresponding pseudo RGB images: sensitivity (SE), specificity (SP), balanced accuracy (BACC), precision (PREC), F_1 score, and intersection-over-union (IoU). Each metric ranges from 0 to 1, where 0 indicates the worst performance and 1 indicates the best performance. Sensitivity, also known as recall and true positive rate, is defined as:

$$SE = \frac{TP}{TP + FN}$$

where *TP* denotes the number of true positives (correctly diagnosed cancerous pixels) and *FN* denotes the number of false negatives (incorrectly diagnosed cancerous pixels). Specificity, also known as selectivity and true negative rate, is defined as:

$$SP = \frac{TN}{TN + FP}$$

where *TN* denotes the number of true negatives (correctly diagnosed non-cancerous pixels) and *FP* denotes the number of false positives (incorrectly diagnosed non-cancerous pixels). Precision, also known as positive predicted value, is defined as:

$$PREC = \frac{TP}{TP + FP}$$

F_1 score, also known as the Dice coefficient, is the harmonic mean of precision and sensitivity defined as:

$$F_1 = \frac{2 \times TP}{2 \times TP + FP + FN}$$

IoU, also referred to as the Jaccard index, is defined as:

$$IoU = \frac{TP}{TP + FP + FN} = \frac{F_1}{2 - F_1}.$$

3.4. Results

3.4.1. Grassmann manifold semi-supervised classifier

We present in Table 3 results of the ablation study aimed to select the optimal configuration for Grassmann manifold approach to semi-supervised pixel-wise classification of HSIs. As commented in section 2.3.1, from the requirement on subspace dimension $d << b$ it is evident that the Grassmann manifold concept is not applicable to pixel-wise classification of pseudo RGB images where $b = 3$. As emphasized in section 2.3.1, the Algorithm 1 can be applied directly on selected spectral pixels but also on their spatial averages estimated from 5 × 5 patches around each pixel. Furthermore, the Algorithm 1 can also be applied to spatial-spectral features extracted by the TensorSSA method [30] and MPRI method [51]. In conducted ablation study we fixed the number of labels per category for estimation of Grassmann points (bases of susbpaces representing cancerous and non-cancerous groups) to 0.5 %. Results reported in Table 3 represent micro performances. However, statistical significance analysis was conducted on image-based performance sequences. We assessed statistical significance between the two classifiers using the Wilcoxon rank-sum test. The null hypothesis of the test assumes that the data come from continuous distributions with equal medians at a 5 % significance level. A p-value less than 0.05 indicates rejection of the null hypothesis. As can be seen in Table 3, configuration which combines Grassmann manifold approach with the TensorSSA 3D spectral-spatial features yields the best performance. It is also statistically significantly better than performance achieved on spectral features and MPRI features. It is better, but not statistically

Table 3
Micro performance metric for Grassman manifold approach to semi-supervised pixel-wise classification of HSIs with 0.5 % of labeled pixels per-group. The best results are in bold. Wilcoxon test is conducted against the best method with corresponding p-values reported in a row below performance metrics.

Spatial average	Spectral	TensorSSA	MPRI	BACC	F_1	IoU	PREC	CPU [min/patch]
–	+	–	–	0.801	0.774	0.631	0.776	0.061
				2.98×10^{-10}	2.98×10^{-10}	2.98×10^{-10}	2.98×10^{-10}	
+	+	–	–	0.943	0.937	0.881	0.934	0.474
				6.20×10^{-4}	1.54×10^{-4}	1.54×10^{-4}	5.2×10^{-3}	
–	–	+	–	**0.956**	**0.951**	**0.907**	**0.950**	3.37
+	–	+	–	0.952	0.947	0.899	0.943	3.87
				0.213	0.078	0.078	0.128	
–	–	–	+	0.878	0.864	0.761	0.866	12.89
				3.03×10^{-10}	3.03×10^{-10}	3.03×10^{-10}	3.03×10^{-10}	
+	–	–	+	0.948	0.942	0.890	0.940	23.66
				0.005	0.002	0.002	0.031	

significant, from performance achieved by combination of spatial averaging and TensorSAA features. This is result is in agreement with intuition because 3D spectral-spatial TensorSAA features already contain pixel-wise local information. Thus, the additional spatial averaging step only deteriorates classification performance. We want to emphasize that micro BACC in the amount of 95.10 % achieved by Grassman-TensorSSA classifier can be considered virtually perfect giving the fact that the pixel-wise ground truth is obtained with the inter-annotator agreement of $\kappa = 0.754$, see section 2.2.2. To provide additional information on quality of Grassmann-TensorSSA classifier, we present in Table 4 classification performance as a function of percentage of labeled pixels per category. By increasing number of labeled pixels per category to 1 %, the micro BACC achieves the amount of 96.3 %.

3.4.2. *Label propagation semi-supervised classifier*

In this section, we conducted a study to validate performance of the SSL-MPRI and SSL-TensorSSA classifiers, as well as to compare them with the k-NN-MPRI, SVM-TensorSSA and standard SSL-spectral classifiers for both HSIs and corresponding pseudo RGB images. For each patch, 1 % and 2 % of pixels per class were labeled to train the SSL-based classifiers. For comparison, k-NN-MPRI and linear SVM-TensorSSA classifiers were trained using 20 % and 5 % of labeled pixels per class, respectively. The reason for using the greater number of labeled pixel per class for training was to achieve decent performance by the k-NN-MPRI and linear SVM-TensorSSA classifiers in conducted analysis. The results of this study are presented in Table 5, focusing on micro performance. For both HSIs and corresponding pseudo RGB images, the SSL-MPRI classifier, using 2 % labeled pixels per class, achieved the highest BACC, F_1 score, and IoU. This performance was superior to the k-NN-MPRI classifier and the SVM-TensorSSA classifier. It also outperformed the SSL-spectral classifier applied to both HSIs and RGB images. It is however important to notice that micro BACC of the SSL-MPRI classifier was 93.6 % with 2 % of labels pixels per class, while Grassmann-TensorSSA classifier achieved micro BACC of 96.3 % with 1 % of labeled pixels per class only. Thus, we prefer to use the Grassmann-TensorSSA classifier for pixel-wise classification of HSIs, and SSL-MPRI classifier for pixel-wise classification of pseudo RGB images. We show in Table 6, performance of SSL-MPRI and SSL-TensorSSA classifiers using only 1 % of labeled pixels per class for training. These results ought to be compared with the results of Grassmann-TensorSSA classifier in Table 4. For SSL-MPRI and SSL-TensorSSA classifiers, we report in Table 7 performance metrics as mean ± standard deviation, calculated on an image-by-image basis. This approach allows for the evaluation of statistical significance between performance on HSIs and their corresponding pseudo RGB images. As shown, both classifiers achieve statistically significant improvements on HSIs compared to pseudo RGB images across all performance metrics. On HSIs, the Grassmann-TensorSSA classifier achieves a statistically significant performance improvement over the SSL-MPRI and SSL-TensorSSA classifiers, see Table 8. Moreover, it is approximately three times faster than the SSL-TensorSSA classifier and it is approximately nine time faster than the SSL-MPRI classifier.

We illustrate in Fig. 7 classification results of Grassmann-TensorSSA, SSL-MPRI and SSL-TensorSAA classifiers on one selected HSI and corresponding pseudoRGB image. As, notified before Grassmann manifold approach is not applicable to pseudo RGB images.

For deep networks, we provided in Table 9 the mean and standard deviation obtained over 10 runs. Data partition into 63 % for training (17 images) and 37 % for testing (10 images) was fixed through all runs. The best performance overall is achieved by the nn-Unet, but there is no difference between HSIs and pseudo RGB images. In comparison with the Grassmann-TensorSSA classifier the performance, depending on the metrics, is 5 %–12 % worse. It is interesting that Grassmann manifold approach with only 0.12 % of labeled pixels-per-class achieved micro BACC of 0.926, see Tables 4 and in comparison with 0.890 achieved by the nn-Unet classifier.

According to our understanding, the main reason why deep networks failed to achieve significantly better performance on HSIs in comparison with the pseudo RGB images is heterogeneity of HSI dataset caused by experimental variations known as batch effects [64]. We show in Fig. 8 pseudo RGB images of six patients that illustrate our claim. These effects can be significantly reduced by means of the stain normalization algorithms [65]. However, to the best of our knowledge, there are no stain normalization methods yet developed for reduction of batch effects in hyperspectral images. Therefore, to make comparison between HSIs and pseudo RGB images fair, we did not apply stain normalization procedure on pseudo RGB images. As opposed to deep networks, proposed Grassmann-TensorSSA semi-supervised classifier is able to adapt to local spectral variations by working on the patches of the size of 238×250 pixels.

Table 4
Micro performance of the Grassman-TensorSSA semi-supervised classification method vs. percentage (%) of labeled pixels per-group.

[%]	SE	SP	BACC	F_1	IoU	PPV	CPU [min/patch]
1	0.961	0.964	0.963	0.959	0.920	0.956	3.46
0.5	0.953	0.960	0.956	0.951	0.907	0.950	3.37
0.25	0.938	0.946	0.942	0.935	0.879	0.933	3.39
0.12	0.921	0.932	0.926	0.919	0.850	0.917	3.42
0.05	0.892	0.908	0.900	0.890	0.801	0.887	3.48

4. Discussion

Efficacy of intraoperative tumor resection directly affects life expectancy, i.e., the resection margin has been known as a powerful predictor of the 5-year survival rate. Traditionally, computational pathology has relied on RGB images of frozen tissue sections, which limits information to the visual range and excludes the data across the continuous spectral range. To address this limitation, HSI technology is

Table 5
Micro performance metrics for the k-NN-MPRI, SVM-TensorSSA, SSL-spectral, SSL-MPRI and SSL-TensorSSA algorithms vs. percentage of labeled pixels-per-class. Evaluation on 27 HSIs and pseudo RGB images. Patch size 230 × 258 pixels.

Algorithm	Percent/Image	SE	SP	BACC	F_1	IoU	PREC.	CPU [min/patch]
k-NN-MPRI	20 HSI	0.912	0.934	0.927	0.919	0.850	0.919	56.72
	RGB	0.862	0.887	0.875	0.862	0.757	0.861	15.95
SVM-TensorSSA	5 HSI	0.892	0.896	0.894	0.883	0.790	0.874	3.38
	RGB	0.886	0.889	0.887	0.876	0.779	0.866	0.10
SSL-Spectral	2 HSI	0.911	0.902	0.907	0.897	0.812	0.883	17.27
	RGB	0.870	0.854	0.862	0.848	0.737	0.823	2.07
SSL-MPRI	2 HSI	0.944	0.930	0.936	0.929	0.867	0.915	16.07
	RGB	0.887	0.878	0.883	0.870	0.771	0.854	8.18
SSL-TensorSSA	2 HSI	0.916	0.907	0.911	0.902	0.821	0.888	15.75
	RGB	0.870	0.858	0.868	0.855	0.747	0.883	1.75

Table 6
Micro performance metrics for the SSL-MPRI and SSL-TensorSSA classifiers for 1 % of labeled pixels-per-class. Evaluation on 27 HSIs and pseudo RGB images. Patch size 230 × 258 pixels.

Algorithm	Image	SE	SP	BACC	F_1	IoU	PREC.	CPU [min/patch]
SSL-MPRI	HSI	0.940	0.923	0.931	0.924	0.858	0.908	29.60
	RGB	0.887	0.878	0.883	0.870	0.771	0.854	11.82
SSL-TensorSSA	HSI	0.911	0.900	0.906	0.896	0.811	0.880	10.25
	RGB	0.875	0.854	0.864	0.851	0.779	0.829	1.48

Table 7
Macro performance metrics for the SSL-MPRI and SSL-TensorSSA classifiers for 1 % of labeled pixels-per-class. Evaluation on 27 HSIs and pseudo RGB images. Wilcox rank-sum test of statistical significance within 95 % confidence interval (p-value). Last row represents statistical significance between SSL-MPRI and SSL-TensorSSA classifiers on HSIs.

Algorithm	Image	SE	SP	BACC	F_1	IoU	PREC.
SSL-MPRI p-value	HSI	0.940 ± 0.013	0.918 ± 0.026	0.929 ± 0.015	0.921 ± 0.014	0.854 ± 0.024	0.903 ± 0.023
	RGB	0.888 ± 0.023	0.874 ± 0.025	0.881 ± 0.019	0.862 ± 0.037	0.759 ± 0.056	0.841 ± 0.068
		5.28×10^{-10}	5.25×10^{-7}	8.78×10^{-10}	1.94×10^{-9}	1.94×10^{-9}	2.43×10^{-3}
SSL-TensorSSA p-value	HSI	0.913 ± 0.020	0.895 ± 0.028	0.904 ± 0.020	0.892 ± 0.021	0.805 ± 0.034	0.873 ± 0.037
	RGB	0.877 ± 0.030	0.851 ± 0.031	0.864 ± 0.024	0.844 ± 0.043	0.732 ± 0.062	0.817 ± 0.074
		3.85×10^{-6}	4.45×10^{-5}	1.07×10^{-7}	4.19×10^{-6}	4.19×10^{-6}	2.00×10^{-3}
p-value		8.20×10^{-7}	3.70×10^{-3}	1.03×10^{-5}	2.14×10^{-6}	2.14×10^{-6}	4.60×10^{-3}

Table 8
Micro performance metrics for the Grassmann-TensorSSA classifier, SSL-MPRI and SSL-TensorSSA classifiers for 1 % of labeled pixels-per-class. Evaluation on 27 HSIs. Wilcox rank-sum test of statistical significance within 95 % confidence interval (p-value) against Grassman-TensorSSA classifier.

Classifier	SE	SP	BACC	F_1	IoU	PPV	CPU [min/patch]
Grassman-TensorSSA	0.961	0.964	0.963	0.959	0.920	0.960	3.46
SSL-MPRI p-value	0.940	0.923	0.931	0.924	0.858	0.908	29.6
	1.39×10^{-8}	9.01×10^{-8}	3.65×10^{-9}	9.11×10^{-10}	9.11×10^{-10}	9.11×10^{-10}	
SSL-TensorSSA p-value	0.911	0.900	0.906	0.896	0.811	0.880	10.25
	6.57×10^{-10}	8.17×10^{-10}	3.89×10^{-10}	3.03×10^{-10}	3.03×10^{-10}	3.03×10^{-10}	

increasingly being used in various medical imaging applications, including computational pathology. However, application of HSI in computational pathology faces three challenges: (1) a shortage of pixel-wise annotated HSI data necessary for training machine learning and DL models; (2) in many cases, the advantages of HSI over traditional RGB imaging have not been conclusively demonstrated, particularly for specimens collected intraoperatively; (3) experimental variability in slide preparation process, also known as batch effects [64], transfers to spectrum variability. That, in combination with the lack of annotated data, makes training of deep networks challenging. To address first two challenges we created a database consisted of 27 HSIs of H&E stained frozen sections, collected from 14 patients with colon adenocarcinoma metastasized to the liver. To overcome third challenge, we combined Grassmann-manifold approach with spectral-spatial features extracted by tensor singular spectrum analysis method for pixel-wise classification of cancerous and non-cancerous pixels. While proposed approach achieved highly competitive performance in intraoperative tumor demarcation problem it still demands involvement of the human expert to label a small amount pixels as cancerous and non-cancerous (0.5 % per class or less). Our future efforts will be directed towards: (*i*) fully automation of the tumor demarcation problem through usage of some state-of-the-art subspace clustering methods [66], to generate initial small amount of high-quality pseudo labels for Grassmann-TensorSSA classifier. (*ii*) fine tuning SpectralGPT foundation model [67] trained on remote sensing hyperspectral data and apply it to interactive tumor demarcation problem.

5. Conclusion

In this work, we addressed intraoperative tumor resection problem through pixel-wise classification of HSIs of H&E stained specimens of metastatic colon cancer in the liver. By using only 1 % of labeled pixels per class (cancer vs. non-cancer) generated locally (on the patch level), the Grassmann-TensorSSA classifier achieved a micro balanced accuracy

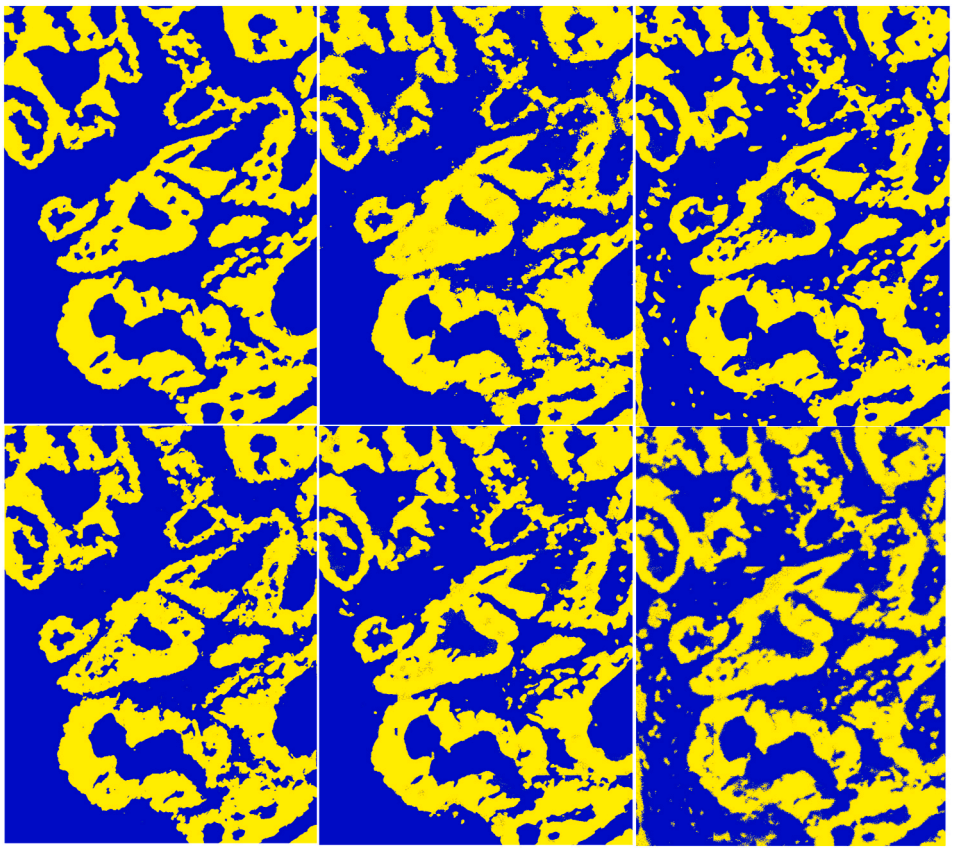

Fig. 7. Top: (left) ground truth image; (middle and right) results of the SSL-MPRI and SSL-TensorSSA classifiers on HSI for 1 % of labeled pixels per class. Bottom: (left) results of Grassmann-TensorSSA classifier on HSI for 0.5 % of labeled pixels per class; (middle and right) results of the SSL-MPRI and SSL-TensorSSA classifiers corresponding pseudo RGB image, shown in Fig. 4, (left). Yellow color denotes pixels classified as cancerous, blue color denotes pixels classified as non-cancerous. For Grassmann-TensorSSA, SSL-MPRI and SSL-TensorSSA, the balanced accuracy in respective order for HSIs is: 0.955, 0.930, 0.860, and for pseudo RGB 0.889 and 0.870. Value of Dice coefficient for HSI in respective order is: 0.947, 0.918, 0.839, and for pseudo RGB 0.870 and 0.832. (For interpretation of the references to color in this figure legend, the reader is referred to the Web version of this article.)

Table 9
Micro performance metrics for deep-neural networks (DNN) averaged over 10 runs. Evaluation on 10 hyperspectral and pseudo RGB images from the test set. Data partition into 63 % for training (17 images) and 37 % for testing (10 images) was fixed through all runs.

DNN	Image	SE	SP	BACC	F_1	IoU	PREC.
DLabv3+	HSI	0.896 ± 0.025	0.829 ± 0.048	0.862 ± 0.019	0.852 ± 0.019	0.742 ± 0.028	0.814 ± 0.040
	RGB	0.881 ± 0.021	0.853 ± 0.022	0.867 ± 0.003	0.855 ± 0.003	0.742 ± 0.004	0.832 ± 0.019
Unet	HSI	0.888 ± 0.073	0.769 ± 0.114	0.828 ± 0.037	0.820 ± 0.033	0.696 ± 0.048	0.773 ± 0.086
	RGB	0.867 ± 0.014	0.866 ± 0.018	0.866 ± 0.006	0.854 ± 0.007	0.746 ± 0.009	0.842 ± 0.016
Unet++	HSI	0.901 ± 0.091	0.784 ± 0.058	0.842 ± 0.030	0.831 ± 0.037	0.712 ± 0.052	0.788 ± 0.037
	RGB	0.853 ± 0.027	0.879 ± 0.016	0.866 ± 0.008	0.853 ± 0.010	0.744 ± 0.015	0.854 ± 0.014
MAnet	HSI	0.919 ± 0.022	0.800 ± 0.034	0.856 ± 0.012	0.851 ± 0.011	0.740 ± 0.017	0.792 ± 0.025
	RGB	0.851 ± 0.002	0.876 ± 0.013	0.864 ± 0.005	0.850 ± 0.006	0.740 ± 0.009	0.850 ± 0.012
UwU-Net	HSI	0.952 ± 0.037	0.733 ± 0.065	0.843 ± 0.021	0.837 ± 0.018	0.720 ± 0.026	0.749 ± 0.041
	RGB	0.791 ± 0.056	0.864 ± 0.051	0.828 ± 0.012	0.809 ± 0.017	0.679 ± 0.022	0.831 ± 0.039
nn-Unet	HSI	0.921 ± 0.021	0.860 ± 0.049	0.890 ± 0.029	0.865 ± 0.083	0.763 ± 0.112	0.827 ± 0.126
	RGB	0.885 ± 0.046	0.901 ± 0.029	0.891 ± 0.030	0.872 ± 0.046	0.772 ± 0.061	0.865 ± 0.084

(BACC) of 0.963 and a micro F1-score of 0.959 on the HSI dataset. In comparison, the performance on corresponding pseudo RGB images achieved by the SSL-MPRI classifier was 0.881 and 0.869, in respective order. The improvements relative to RGB images are statistically significant in six classification performance metrics. The Grassmann-TensorSSA approach also outperformed the SSL-MPRI approach as well as six DL architectures trained with 63 % of labeled pixels. Moreover, DL architectures achieved on HSIs classification performance no better than the one on corresponding pseudo RGB images. Based on computation times reported in Tables 3 and 4 it is evident that software efficient implementation can enable to process the hyperspectral image with the size of 1384 × 1035 × 351 within the time frame of 5 min. Thus, we conclude that Grassmann-TensorSSA classifier in combination with HSI represents state-of-the-art solution for intraoperative computation of tumor resection margin.

CRediT authorship contribution statement

Ivica Kopriva: Writing – review & editing, Writing – original draft, Visualization, Supervision, Software, Project administration, Methodology, Formal analysis, Conceptualization. **Dario Sitnik:** Software, Methodology. **Laura-Isabelle Dion-Bertrand:** Data curation. **Marija**

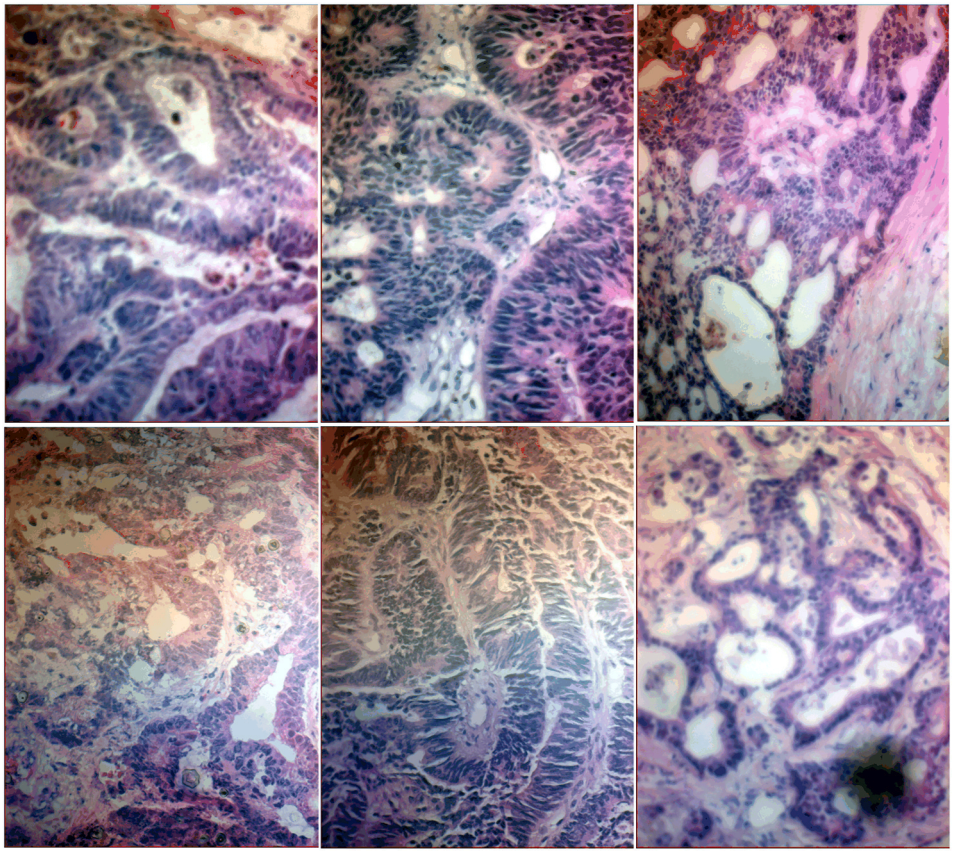

Fig. 8. Pseudo RGB images of histopathological specimens collected from six patients. Color (spectra) variations due to batch effects cause difficulties of training deep networks. (For interpretation of the references to color in this figure legend, the reader is referred to the Web version of this article.)

Milković Periša: Data curation. **Arijana Pačić:** Data curation. **Mirko Hadžija:** Data curation. **Marijana Popović Hadžija:** Data curation.

Ethics statement

The Institutional Review Board of Clinical Hospital Dubrava approved the collection of samples on May 24, 2016. All patients provided written informed consent, and the data were anonymized.

Declaration of generative AI and AI-assisted technologies in the writing process

During the preparation of this work the author(s) used ChatGPT in order to improve readability and language. After using this tool/service, the author(s) reviewed and edited the content as needed and take(s) full responsibility for the content of the publication.

Declaration of competing interest

The authors declare the following financial interests/personal relationships which may be considered as potential competing interests: Ivica Kopriva reports financial support was provided by Croatian Science Foundation. If there are other authors, they declare that they have no known competing financial interests or personal relationships that could have appeared to influence the work reported in this paper.

Acknowledgments

This work was supported by the Croatian Science Foundation under project number HRZZ-IP-2022-10-6403.

Data availability

All data used for this research are public on data repository https://data.fulir.irb.hr/islandora/object/irb:538. Implementation of semi-supervised learning based experiments is available at https://github.com/ikopriva/ColonCancerHSI.

References

[1] D. Sitnik, G. Aralica, M. Hadžija, M. Popović Hadžija, A. Pačić, M. Milković Periša, L. Manojlović, K. Krstanac, A. Plavetić, I. Kopriva, A dataset and a methodology for intraoperative computer-aided diagnosis of a metastatic Colon cancer in a liver, Biomed. Signal Process Control 66 (2021) e102402, https://doi.org/10.1016/j.bspc.2020.102402.

[2] D. Ravi, H. Fabelo, G. Marrero Callico, G.Z. Yang, Manifold embedding and semantic segmentation for intraoperative guidance with hyperspectral brain imaging, IEEE Trans. Med. Imag. 36 (9) (2017) 1845–1857, https://doi.org/10.1109/TMI.2017.2695523.

[3] D. Pertzborn, H.-N. Nguyen, K. Hüttman, J. Prengel, G. Ernst, O. Guntinas-Lichius, F. von Eggeling, F. Hoffman, Intraoperative assessment of tumor margins in tissue sections with hyperspectral imaging and machine learning, Cancers 15 (1) (2022) 213, https://doi.org/10.3390/cancers15010213.

[4] Emory Healthcare. Tumor resection. Retrieved from, https://www.emoryhealthcare.org/centers-programs/orthopaedic-oncology/treatments/tumor-resection (accessed 10 March 2025).

[5] T.Y. Chen, L.J. Emrich, D.J. Driscoll, The clinical significance of pathological findings in surgically resected margins of the primary tumor in head and neck carcinoma, Int. J. Radiat. Oncol. Biol. Phys. 13 (6) (1987) 833–837, https://doi.org/10.1016/0360-3016(87)90095-2.

[6] A. Binhamed, R.W. Nason, A.A. Abdoh, The clinical significance of the positive surgical margin in oral cancer, Oral Oncol. 43 (8) (2007) 780–784, https://doi.org/10.1016/j.oraloncology.2006.10.001.

[7] S. Trajanovski, C. Shan, P.J.C. Weijtmansm, S.G. Brouwer de Koning, T.J.M. Ruers, Tongue tumor detection in hyperspectral images using deep learning semantic segmentation, IEEE Trans. Biomed. Eng. 68 (4) (2020) 1330–1340, https://doi.org/10.1109/TBME.2020.3026683.

[8] S. Ortega, M. Halicek, H. Fabelo, G.M. Callico, B. Fei, Hyperspectral and multispectral imaging in digital and computational pathology: a systematic review,

biomed, Opt. Express 11 (6) (2020) 3195–3232, https://doi.org/10.1364/BOE.386338.
[9] N. Clancy, G. Jones, L. Maier-Hein, D.S. Elson, D. Stoyanov, Surgical spectral imaging, Med. Image Anal. 63 (2020) e101699, https://doi.org/10.1016/j.media.2020.101699.
[10] G. Lu, B. Fei, Medical hyperspectral imaging: a review, J. Biomed. Opt. 19 (1) (2014) e10901, https://doi.org/10.1117/1.JBO.19.1.010901.
[11] Q. Li, X. He, Y. Wang, H. Liu, D. Xu, F. Guo, Review of spectral imaging technology in biomedical engineering: achievements and challenges, J. Biomed. Opt. 18 (2013) 100901, https://doi.org/10.1117/1.JBO.18.10.100901.
[12] N. Kumar, P. Uppala, K. Duddu, H. Sreedhar, V. Varma, G. Guzman, M. Walsh, A. Sethi, Hyperspectral tissue image segmentation using semi-supervised NMF hierarchical clustering, IEEE Trans. Med. Imag. 38 (5) (2019) 1304–1313, https://doi.org/10.1109/TMI.2018.2883301.
[13] X. Xie, Y. Wang, Q. Li, S^3R: self-Supervised spectral regression for hyperspectral histopathology image classification, in: 25th International Conference on Medical Image Computing and Computer Assisted Intervention (MICCA), 2022, pp. 46–55, https://doi.org/10.1007/978-3-031-16434-7_5.
[14] L. Sun, M. Zhou, Q. Li, M. Hu, Y. Wen, J. Zhang, Y. Lu, J. Chu, Diagnosis of cholangiocarcinoma from microscopic hyperspectral pathological dataset by deep convolution neural networks, Methods 202 (2022) 22–30, https://doi.org/10.1016/j.ymeth.2021.04.005.
[15] Y. Zhang, Y. Wang, B. Zhang, Q. Li, A hyperspectral dataset of precancerous lesions in gastric cancer and benchmarks for pathological diagnosis, J. Biophot. 15 (2022) e202200163, https://doi.org/10.1002/jbio.202200163.
[16] E. Zharkikh, V. Dremin, E. Zherebtsov, A. Dunaev, I. Melinski, Biophotonics methods for functional monitoring of complications of diabetes mellitus, J. Biophot. 13 (2020) e202000203, https://doi.org/10.1002/jbio.202000203.
[17] L. Ma, J.V. Little, A.C. Chen, L. Myers, B.D. Sumer, B. Fei, Automatic detection of head and neck squamous cell carcinoma on histologic slides using hyperspectral microscopic imaging, J. Biomed. Opt. 27 (4) (2022) e046501, https://doi.org/10.1117/1.JBO.27.4.046501.
[18] A. Pardo, E. Renal, V. Krishnaswamy, J.M. Lopez-Higuera, B.W. Pogue, O. M. Conde, Directional kernel density estimation for classification of breast tissue spectra, IEEE Trans. Med. Imag. 36 (1) (2017) 64–73, https://doi.org/10.1109/TMI.2016.2593948.
[19] L.C.G. Peraza Herrera, C. Horgan, S. Ourselin, M. Ebner, T. Vercauteren, Hyperspectral image segmentation: a preliminary study on the oral and dental spectral image base (ODSI-DB), Comput. Methods Biomech. Biomed. Eng.: Imag. & Vis. 11 (4) (2023) 1290–1298, https://doi.org/10.1080/21681163.2022.2160377.
[20] W. Zeng, W. Li, R. Tao, R. Ianet, Important-aware network for microscopic hyperspectral pathology image segmentation, in: International Congress on Image and Signal Processing, Biomedical Engineering and Informatics (CISP-BMEI), November, 2022, pp. 5–7, https://doi.org/10.1109/CISP-BMEI56279.2022.9979919. Beijing, China.
[21] S.M. Borzov, O.I. Potaturkin, Spectral-spatial methods for hyperspectral image classification, review, Autom. Monit. Meas. 54 (6) (2018) 582–599, https://doi.org/10.3103/S8756699018060079.
[22] A. Schröder, M. Maktabi, R. Thieme, B. Jansen-Winkeln, I. Gockel, C. Chalopin, Evaluation of artificial neural networks for the detection of esophagus tumor cells in microscopic hyperspectral image, in: 2022 25th Euromicro Conference on Digital System Design (DSD), 2022, pp. 827–834, https://doi.org/10.1109/DSD57027.2022.00116.
[23] U. Cinar, R. Cetin Atalay, Y. Yardimici Cetin, Human hepatocellular carcinoma classification from H&E stained histopathology images with 3D convolutional neural networks and focal loss function, J. Imaging 9 (2023) 25, https://doi.org/10.3390/jimaging9020025.
[24] S. Ortega, L. Quintana-Quintana, R. Leon, H. Fabelo, M. de la Luz Plaza, R. Camacho, G.M. Callico, Histological hyperspectral glioblastoma dataset (HistologyHSI-GB), Sci. Data 11 (2024) 681, https://doi.org/10.1038/s41597-024-03510-x.
[25] Q. Zhang, Q. Li, G. Yu, L. Sun, M. Zhou, J. Chu, A multidimensional choledoch database and benchmarks for cholangiocarcinoma diagnosis, IEEE Access 7 (2019) 149414, https://doi.org/10.1109/ACCESS.2019.2947470.
[26] S. Ortega, G.M. Gallico, M.L. Plaza, R. Camacho, H. Fabelo, R. Sarmiento, Hyperspectral database of pathological In-Vitro human brain samples to detect carcinogenic tissues, in: 2016 IEEE 13th International Symposium on Biomedical Imaging (ISBI), 2016, pp. 369–372, https://doi.org/10.1109/ISBI.2016.7493285.
[27] M. Lv, T. Chen, Y. Yang, T. Tu, N. Zhang, W. Li, Membranous nephropathy classification using microscopic hyperspectral imaging and tensor patch-based discriminative linear regression, Biomed. Opt. Express 12 (5) (2021) 2968–2978, https://doi.org/10.1364/BOE.421345.
[28] S. Ortega, M. Halicek, H. Fabelo, R. Camacho, M.L. de la Plaza, F.M. Godtliebsen, G. Callicó, B. Fei, Hyperspectral imaging for the detection of glioblastoma tumor cells in H&E slides using convolutional neural networks, Sensors 20 (2020) 1911, https://doi.org/10.3390/s20071911.
[29] T. Wu, W.U. Bajwa, Leraning the nonlinear geometry of high-dimensional data: models and algorithms, IEEE Trans. Signal Process. 63 (23) (2015) 6229–6244, https://doi.org/10.1109/TSP.2015.2469637.
[30] P.A. Absil, R.E. Mahony, R. Sepulchre, Optimization Algorithms on Matrix Manifolds, Princeton University Press, 2008.
[31] H. Fu, G. Sun, A. Zhang, B. Shao, J. Ren, X. Jia, Tensor singular spectrum analysis for 3-D feature extraction in hyperspectral image, IEEE Trans. Geosci. Rem. Sens. 61 (2023) e5403914, https://doi.org/10.1109/TGRS.2023.3272669.
[32] W.K. Ma, J.M. Bioucas-Dias, J. Chanussot, P. Garder, Signal and image processing in hyperspectral remote sensing, IEEE Signal Process. Mag. 31 (1) (2014) 22–23, https://doi.org/10.1109/MSP.2013.2282417.
[33] S. Puustinen, J. Hyttinen, G. Hisuin, H. Vrzáková, A. Houtarinen, P. Fält, Towards clinical hyperspectral imaging (HSI) standards: initial design for a microneurosurgical HSI database, in: 2022 IEEE 35th International Symposium on Computer-based Medical Systems (CBMS), 2022, pp. 394–399, https://doi.org/10.1109/CBMS55023.2022.00077.
[34] F.B. Muniz, M. de F.O. Baffa, L. Bachman, J.C. Felipe, Histopathological diagnosis of Colon cancer using micro-FTIR hyperspectral imaging and deep learning, Comput. Methods Progr. Biomed. 231 (2023) e107388, https://doi.org/10.1016/j.cmpb.2023.107388.
[35] S. Blais-Ouellete, Method and Apparatus for a Bragg Grating Tunable Filter, 2009. US-20050195484-A1.
[36] M. Magnusson, J. Sigurdsson, S.E. Armasson, M.O. Ulfarsson, H. Deborah, J. E. Sveinsson, Creating RGB images from hyperspectrall images using a color matching function, in: IGARSS 2020 - 2020 IEEE International Geoscience and Remote Sensing Symposium, 2020, pp. 2045–2048, https://doi.org/10.1109/IGARSS39084.2020.9323397.
[37] R. Colling, H. Pitman, K. Oien, N. Rajpoot, P. Macklin, D. Snead, T. Sackville, C. Verrill, C., artificial intelligence in digital pathology: a roadmap to routine use in clinical practice, J. Pathol. 249 (2) (2019) 143–150, https://doi.org/10.1002/path.5310.
[38] J.L. Fleiss, Measuring nominal scale agreement among many raters, Psychol. Bull. 76 (5) (1971) 378–382, https://doi.org/10.1037/h0031619.
[39] J.R. Landis, G.G. Koch, The measurement of observer agreement for categorical data, Biometrics 33 (1) (1977) 159–174, https://doi.org/10.2307/2529310.
[40] B. Wang, Y. Hu, J. Gao, Y. Sun, F. Ju, B. Yin, Learning adaptive neighborhood graph on grassmann manifolds for Video/image-set subspace clustering, IEEE Trans. Multimed. 23 (2020) 216–227, https://doi.org/10.1109/TMM.2020.2975394.
[41] B. Wang, Y. Hu, J. Gao, Y. Sun, F. Ju, B. Yin, Adaptive fusion of heterogeneous manifolds for subspace clustering, IEEE Transact. Neural Networks Learn. Syst. 32 (8) (2021) 3484–3497, https://doi.org/10.1109/TNNLS.2020.3011717.
[42] B. Wang, Y. Hu, J. Gao, Y. Sun, B. Yin, Localized LRR on grassmann manifold: an extrinsic view, IEEE Trans. Circ. Syst. Video Technol. 28 (10) (2018) 2524–2536, https://doi.org/10.1109/TCSVT.2017.2757063.
[43] X. Shen, H. Krim, Y. Gu, Beyond union of subspaces: Subspace pursuit on grassmann manifolds for data representation, in: 2016 IEEE International Conference on Acoustics, Speech and Signal Processing (ICASP 2016), 2016, pp. 4079–4081, https://doi.org/10.1109/ICASSP.2016.7472444.
[44] R.G. Baraniuk, V. Cevher, M.B. Wakin, Low-dimensional models for dimensionality reduction and signal recovery: a geometric perspective, Proc. IEEE 98 (6) (2010) 959–971, https://doi.org/10.1109/JPROC.2009.2038076.
[45] Y.M. Lu, M.N. Do, A theory of sampling signals from a union of subspaces, IEEE Trans. Signal Process. 56 (6) (2008) 2334–2345, https://doi.org/10.1109/TSP.2007.914346.
[46] Y. Altun, D.A. McAllester, M. Belkin, Margin semi-supervised learning for structured variables, in: NIPS'05: Proceedings of the 18th International Conference on Neural Information Processing Systems, 2005, pp. 33–40.
[47] S.C. Fralick, Learning to recognize patterns without a teacher, IEEE Trans. Inf. Theor. 13 (1) (1967) 57–64, https://doi.org/10.1109/TIT.1967.1053952.
[48] P.A. Traganitis, G.B. Giannakis, Sketched subspace clustering, IEEE Trans. Signal Process. 66 (2018) 1663–1675, https://doi.org/10.1109/TSP.2017.2781649.
[49] X. Yang, Y. Ye, X. Li, R.Y. Lau, X. Zhang, X. Huang, Hyperspectral image classification with deep learning models, IEEE Trans. Geosci. Rem. Sens. 56 (9) (2018) 5408–5423, https://doi.org/10.1109/TGRS.2018.2815613.
[50] M.E. Kilmer, C.D. Martin, Factorization strategies for third-order tensors, Lin. Algebra Appl. 453 (3) (2011) 641–658, https://doi.org/10.1016/j.laa.2010.09.020.
[51] Y. Wei, S. You, L.S. Giraldo, J. Principe, Multiscale principle of relevant information for hyperspectral image classification, Mach. Learn. 112 (2023) 1227–1252, https://doi.org/10.1007/s10994-021-06011-9.
[52] J. Principe, Information Theoretic Learning - Reny's Entropy and Kernel Perspective, Springer, New York, 2010.
[53] S.M. Rao, Unsupervised Learning: an Information Theoretic Framework, University of Florida ProQuest Dissertations & Theses, 2008 3367034.
[54] E. Parzen, On estimation of a probability density function and mode, Ann. Math. Stat. 33 (3) (1962) 1065–1076. https://www.jstor.org/stable/2237880.
[55] T. Bandos, L. Bruzzone, G. Camps-Valls, Classification of hyperspectral images with regularized linear discriminant analysis, IEEE Trans. Geosci. Rem. Sens. 47 (3) (2009) 862–873, https://doi.org/10.1109/TGRS.2008.2005729.
[56] Q. Wang, L. Sun, Y. Wang, M. Zhou, M. Hu, J. Chen, Y. Wen, Q. Li, Identification of melanoma from hyperspectral pathology image using 3D convolutional networks, IEEE Trans. Med. Imag. 40 (1) (2021) 218–227, https://doi.org/10.1109/TMI.2020.3024923.
[57] B. Manifold, S. Men, R. Hu, D. Fu, A versatile deep learning architecture classification and label-free prediction of hyperspectral images, Nat. Mach. Intell. 3 (2021) 306–315, https://doi.org/10.1038/s42256-021-00309-y.
[58] F. Isenses, P.F. Jaeger, S.A.A. Kohl, J. Petersen, K.H. Maier-Hein, nnUnet: a self-configuring method for deep learning-based biomedical image segmentation, Nat. Methods 18 (2021) 203–211, https://doi.org/10.1038/s41592-020-01008-z.
[59] L.-C. Chen, Y. Zhu, G. Papandreou, F. Schroff, H. Adam, Encoder-decoder with atrous separable convolution for semantic image segmentation, in: Proceedings of the European Conference on Computer Vision (ECCV), 2018, pp. 833–851, https://doi.org/10.1007/978-3-030-01234-2_49.

[60] O. Ronneberger, P. Fischer, T. Brox, U-net: convolutional networks for biomedical image segmentation, in: International Conference on Medical Image Computing and computer-assisted Intervention, Springer, 2015, pp. 234–241, https://doi.org/10.1007/978-3-319-24574-4_28.

[61] R. Zhou, M.M. Rahman Siddiquee, N. Tajbakhsh, J. Liang, Unet++: a nested u-net architecture for medical image segmentation, in: Deep Learning in Medical Image Analysis and Multimodal Learning for Clinical Decision Support, Springer International Publishing, 2018, pp. 3–11, https://doi.org/10.1007/978-3-030-00889-5_1.

[62] T. Fan, G. Wang, Y. Li, H. Wang, Ma-net: a multi-scale attention network for liver and tumor segmentation, IEEE Access 8 (179) (2020) 656, https://doi.org/10.1109/ACCESS.2020.3025372, 179.

[63] A. Paszke, S. Gross, F. Massa, A. Lerer, J. Bradbury, G. Chanan, T. Killeen, Z. Lin, N. Gimelshein, L. Antiga, A. Desmaison, A. Köpf, E. Yang, Z. DeVito, M. Raison, A. Tejani, S. Chilamkurthy, B. Steiner, L. Fang, J. Bai, S. Chintala, Pytorch: an imperative style, high-performance deep learning library, in: 2019 Advances in Neural Information Processing Systems (NIPS) vol. 33, 2019, pp. 8026–8037, e721.

[64] M. Gavrilovic, J.C. Azar, J. Lindblad, C. Wählby, E. Bengtsson, C. Busch, I. B. Carlbom, Blind color decomposition of histological images, IEEE Trans. Med. Imag. 32 (6) (2013) 983–994, https://doi.org/10.1109/TMI.2013.2239655.

[65] A. Vahadane, T. Peng, A. Sethi, S. Albarqouni, L. Wang, M. Baust, K. Steiger, A. M. Schlitter, I. Esposito, N. Navab, Structure-preserving color normalization and sparse stain separation for histological images, IEEE Trans. Med. Imag. 35 (2016) 1962–1971, https://doi.org/10.1109/TMI.2016.2529665.

[66] Z. Long, C. Zhu, J. Chen, Z. Li, Y. Ren, Y. Liu, Multi-view MERA subspace clustering, IEEE Trans. Multimed. 26 (2024) 3102–3112, https://doi.org/10.1109/TMM.2023.3307239.

[67] D. Hong, B. Zhnag, X. Li, Y. Li, C. Li, J. Yao, N. Yokoya, H. Li, P. Ghamisi, X. Jia, A. Plaza, P. Gamba, J.A. Benediktsson, J. Chanussot, SpectralGPT: spectral remote sensing foundation model, IEEE Trans. Pattern Anal. Mach. Intell. 8 (2024) 5227–5244, https://doi.org/10.1109/TPAMI.2024.3362475.